

## RESEARCH ARTICLE

## Temporal variability in the Antarctic Polar Front (2002–2014)

10.1002/2016JC012145

Natalie M. Freeman<sup>1</sup>, Nicole S. Lovenduski<sup>1</sup>, and Peter R. Gent<sup>2</sup>

## Key Points:

- Zonally averaged frontal temperature and intensity vary seasonally while latitudinal position does not
- The zonally averaged front has not shifted meridionally but has intensified
- Low congruence between SAM/ENSO and front variability

## Correspondence to:

N. M. Freeman,  
natalie.freeman@colorado.edu

## Citation:

Freeman, N. M., N. S. Lovenduski, and P. R. Gent (2016), Temporal variability in the Antarctic Polar Front (2002–2014), *J. Geophys. Res. Oceans*, 121, 7263–7276, doi:10.1002/2016JC012145.

Received 11 JUL 2016

Accepted 31 AUG 2016

Accepted article online 8 SEP 2016

Published online 3 OCT 2016

Corrected 15 OCT 2016

This article was corrected on 15 OCT 2016. See the end of the full text for details.

<sup>1</sup>Department of Atmospheric and Oceanic Sciences and Institute of Arctic and Alpine Research, Boulder, Colorado, USA,  
<sup>2</sup>Climate and Global Dynamics Laboratory, National Center for Atmospheric Research, Boulder, Colorado, USA

**Abstract** We investigate intraannual to interannual variability in the Antarctic Polar Front (PF) using weekly PF realizations spanning 2002–2014 (found at doi.pangaea.de/10.1594/PANGAEA.855640). While several PF studies have used gradient maxima in sea surface temperature (SST) or height to define its location, results from this study are based on a PF defined using SST measurements that avoid cloud contamination and the influence of steric sea level change. With a few regional exceptions, we find that the latitudinal position of the PF does not vary seasonally, yet its temperature exhibits a clear seasonal cycle. Consistent with previous studies, the position and intensity of the PF is largely influenced by bathymetry; generally, over steep topography, we find that the front intensifies and interannual variability in its position is low. We also investigate drivers of PF variability in the context of large-scale climate variability on various spatial and temporal scales, but find that the major modes of Southern Hemisphere climate variability explain only a tiny fraction of the interannual PF variance. Over the study time period, the PF intensifies at nearly all longitudes while exhibiting no discernible meridional displacement in its zonal mean path.

## 1. Introduction

The large-scale circulation of the Southern Ocean is largely driven by the overlying westerly winds and buoyancy forcing [Marshall and Speer, 2012]. The strong westerly winds force the eastward-flowing, zonally unbounded Antarctic Circumpolar Current (ACC) and set up a globally significant meridional overturning circulation. Light, surface waters are forced equatorward through Ekman transport and cold, dense, nutrient-rich, carbon-rich, and oxygen-poor waters must upwell from below. Here upwelling water has the opportunity to exchange heat and carbon at the air-sea interface before cooling and sinking to the south to form bottom water or warming and advancing to the north as intermediate and mode water. These pathways help ventilate the global ocean, transporting heat, carbon, nutrients, oxygen, and other oceanic properties [Rintoul et al., 2001; Sarmiento et al., 2004; Sabine et al., 2004; Mignone et al., 2006; Sallée et al., 2012]. While the ACC connects the southern Atlantic, Indian, and Pacific Ocean basins, it also acts as a barrier to poleward heat transport, contributing to the unique and isolated Antarctic climate [Rintoul et al., 2001]. The poleward transport of heat by mesoscale eddies formed within the ACC is likely the only compensation for heat lost during air-sea exchange [de Szoeke and Levine, 1981; Rintoul et al., 2001].

Making up the vast ACC are multiple hydrographic fronts characterized by strong meridional gradients in oceanic properties, formed via eddy-mean flow interaction, and delineating physical and biogeochemical zones [Deacon, 1982; Pollard et al., 2002]. Of these, the Antarctic Polar Front (PF; climatological position shown in Figure 1a) marks the transition between cold, fresh Antarctic water and warmer, saltier sub-Antarctic waters as well as the boundary between nutrient-rich and nutrient-poor waters [Pollard et al., 2002; Sarmiento et al., 2004]. The position of the PF has implications for the physical and biogeochemical state of the Southern Ocean, as shifts in the location could cause changes in eddy heat fluxes, air-sea fluxes, basin temperature, biological productivity, or biogeography [Ansorge et al., 2014; Swart and Speich, 2010; Gille, 2002; Moore and Abbott, 2000; Pollard et al., 2002]. Yet the temporal variability and long-term trends in the position and strength of the circumpolar PF are still poorly understood, largely due to (a) the paucity of high-resolution, repeat hydrographic data (as in Orsi et al. [1995] and Belkin and Gordon [1996]), (b) cloud contamination of infrared satellite coverage (as in Moore et al. [1999]), and (c) disparities between commonly employed PF-identification methods [see Langlais et al., 2011; Graham et al., 2012; Chapman, 2014; Gille, 2014], including those using sea surface height (SSH) data that may be sensitive to the large-scale steric height changes characteristic of climate change [e.g., Sokolov and Rintoul, 2009a].

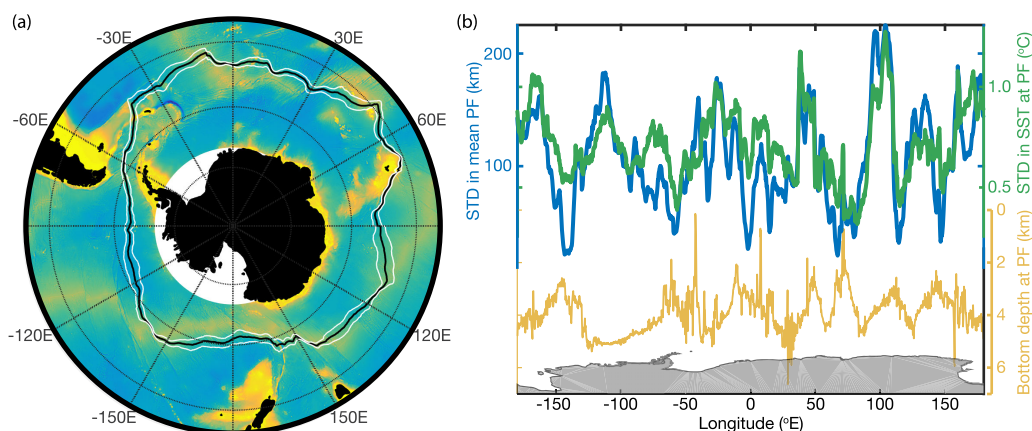


**Figure 1.** (a) Temporal mean (black contour) and standard deviation (white contours indicate  $\pm 1\sigma$ ) in the monthly Polar Front position (June 2002 to February 2014) overlain on predicted seafloor topography obtained from the National Geophysical Data Center ([www.ngdc.noaa.gov/mgg/dat/misc/predicted\\_seafloor\\_topography/TOPO/](http://www.ngdc.noaa.gov/mgg/dat/misc/predicted_seafloor_topography/TOPO/)) [Smith and Sandwell, 1994], where warm colors indicate shallow bathymetry and cool colors, deep. (b) Standard deviation in monthly mean PF position (blue) and anomalous SST at the PF (green) along with bottom depth at the mean PF (yellow).

Using historical hydrographic data, the frontal studies of Orsi *et al.* [1995] and Belkin and Gordon [1996] provided a first look at the mean location and structure of the circumpolar PF, but given the lack of repeat observations, its time-varying properties could not be investigated. Observing both SSH and temperature (SST) via satellite has allowed for the remote detection of fronts at greater temporal and spatial resolution [Gille, 1994; Moore *et al.*, 1999; Sokolov and Rintoul, 2002; Dong *et al.*, 2006].

Several previous studies have used SSH contouring methods to investigate PF variability [see Sokolov and Rintoul, 2002; Sallée *et al.*, 2008; Sokolov and Rintoul, 2009a; Billany *et al.*, 2010; Kim and Orsi, 2014]. Sokolov and Rintoul [2009b] present the spatiotemporal variability of the PF over a 15 year period (1992–2007) and document an observed long-term southward displacement in PF position. Sallée *et al.* [2008] suggest that on regional scales, the PF (1993–2005) shifts in spatially inhomogeneous ways in response to large-scale climate variability. However, SSH-based frontal analyses leave a number of open questions. First, shifts in the position of fixed SSH contours are potentially sensitive to steric sea level rise (i.e., thermal expansion), likely associated with a warming Southern Ocean [Gille, 2002]. Second, Graham *et al.* [2012] highlight that since an SSH contour is not always associated with an enhanced SSH gradient, particularly in regions where fronts weaken or dissipate, tracking these SSH contours alone is insufficient for quantifying variability and change in the PF.

Given the marked temperature gradient at the PF, a few studies have used SST gradient-based definitions to identify its location; methods which are insensitive to steric expansion but previously lacked adequate spatial and temporal resolution. Moore *et al.* [1999] suggest that the PF (1987–1993) exhibits seasonal variability and is greatly influenced by bottom topography. Dong *et al.* [2006] suggest that displacements in the overlying wind position force shifts in the PF. However, Moore *et al.* [1999] utilize infrared SSTs and therefore cannot resolve the PF in any areas contaminated by clouds and, although microwave radiometers can penetrate cloud cover [see Wentz *et al.*, 2000], Dong *et al.* [2006] only investigate the first 3 years (2003–2005) of the cloud-penetrating microwave SST record. Circumventing the above SST and SSH methodological limitations, Freeman and Lovenduski [2016a] map the PF at high spatial and temporal resolution for  $\sim 12$  years of the microwave record.

Here we utilize the first long-term, high-resolution PF data set derived from microwave radiometer-based SST gradients [Freeman and Lovenduski, 2016a,b] to investigate intraannual to interannual variability and trends in the position and strength of the Antarctic Polar Front from 2002 to 2014 and its linkages with the leading patterns of climate variability.

## 2. Data and Methods

Monthly anomalies are computed by removing the long-term climatological monthly mean. To compute seasonal averages, we average over June–August (JJA), September–November (SON), December–February (DJF), and March–May (MAM). Prior to correlation and regression analysis, data sets are detrended by

removing the long-term linear (least squares) trend. Trends are discussed in section 3.3. The statistical significance (at the 95% level) of all reported trends are assessed using the Student's *t* test. We use the method of *Bretherton et al.* [1999] to test the statistical significance of all reported correlation coefficients in the presence of autocorrelation.

### 2.1. Time-Variable Polar Front Properties

*Freeman and Lovenduski* [2016a] construct ~12 years of weekly realizations of PF position (612 weeks spanning 2 June 2002 to 22 February 2014), inferred from gradient maxima in microwave SSTs (Microwave OI SST Remote Sensing Systems product, version 4). The methods presented in their study advance previous PF-identification efforts by avoiding water vapor and cloud contamination [see *Wentz et al.*, 2000] and providing circumpolar realizations at high spatial and temporal resolution; these PF realizations are shown to be consistent with those inferred from bathythermographic data and previously published climatologies. Their comprehensive PF mapping scheme locates regions where the absolute gradient in SST exceeds a 1.5°C change over a 100 km distance, relaxing this gradient criterion in order to ensure spatial and/or thermal continuity. The reader is referred to *Freeman and Lovenduski* [2016a] for a detailed description of the PF mapping technique. In this study, weekly PF data [*Freeman and Lovenduski*, 2016b] retain 0.25° spatial resolution and are averaged to monthly temporal resolution (141 months total).

As in *Freeman and Lovenduski* [2016a], the variables *SST* and  $\Delta$ *SST at the PF* indicate the SST and absolute SST gradient, respectively, identified at the latitude, longitude, and time of the PF realization. We define the absolute SST gradient as,

$$|\Delta T| = \sqrt{(\delta T / \delta x)^2 + (\delta T / \delta y)^2},$$

where  $\delta T$  is the temperature difference (°C) and  $\delta x$  and  $\delta y$  are the kilometer distances between any two longitude or latitude points, respectively. We further refer to the SST gradient at the PF as the intensity or strength of the PF.

Since zonal mean SST and  $\Delta$ SST at the PF exhibit seasonality (see section 3.1), the seasonal cycle is removed from these variables prior to statistical analysis. As the majority of meridional PF position and intensity do not exhibit seasonal cycles (not shown), the seasonal cycle is only removed from the meridional SST at the PF prior to statistical analysis.

### 2.2. Wind Speed and the Surface Westerly Jet

To determine the role of wind on PF variability, we use merged microwave radiometer wind speed data (representing speeds at 10 m height) processed by Remote Sensing Systems [*Remote Sensing Systems*, 2016]. This wind product is on a 1° grid at monthly temporal resolution and derived from the following satellite radiometers: Special Sensor Microwave Imager (SSM/I F08 through F15), Special Sensor Microwave Imager Sounder (SSMIS F16 and F17), WindSat Polarimetric Radiometer, and Advanced Microwave Scanning Radiometer (AMSR-2). Data processing involves many quality control measures, including the removal of rain-contaminated or sea ice-contaminated wind speeds, post hoc corrections (as described in *Wentz* [2015]), and consideration of differences between instruments (e.g., resolution and look angle). For further details on data processing, the reader is encouraged to visit [www.remss.com/measurements/wind/wspd-1-deg-product](http://www.remss.com/measurements/wind/wspd-1-deg-product).

Between 20°S and 70°S, we define the strength of the surface westerly wind jet as the maximum zonal mean wind speed (m/s); westerly jet position is then defined as the latitude (degrees) of this jet maximum (as in *Swart et al.* [2015]).

### 2.3. Climate Indices

We use the monthly (June 2002 to February 2014) SAM (or Antarctic Oscillation) and Niño-3.4 ENSO indices obtained from the National Oceanic and Atmospheric Administration (NOAA) Climate Prediction Center (CPC; [www.cpc.ncep.noaa.gov](http://www.cpc.ncep.noaa.gov)). The SAM index is defined as the leading principal component of monthly 700 hPa geopotential height anomalies (south of 20°S) from the National Centers for Environmental Prediction/National Center for Atmospheric Research (NCEP/NCAR) reanalysis. Variations in Niño-3.4 are based on SST anomalies averaged over the 5°N–5°S, 170°W–120°W region.

We standardize the SAM and ENSO indices prior to analysis by removing the long-term mean and dividing by the long-term standard deviation. We correlate and regress detrended data variables (see section 2.1 for anomalous data information) onto the given climate index using the method of *Bretherton et al.* [1999] to test the statistical significance of all reported correlation coefficients in the presence of autocorrelation. We quantify the proportion of trends linearly attributable to the SAM and ENSO by regressing the monthly time series onto the detrended indices and multiplying the resulting regression coefficients by the trend in the index; the residuals (i.e., the components of the trend that cannot be linearly attributed to the given index) are quantified by subtracting the linearly congruent components from the original trends (as outlined in *Thompson et al.* [2000]).

### 3. Results

The climatological mean features of the Antarctic Polar Front are discussed in *Freeman and Lovenduski* [2016a]. Figure 1a displays the mean PF path (black contour) and its standard deviation (white contours;  $\pm 1\sigma$  in the monthly PF) overlain on bottom topography. In general, the latitudinal location of the PF is more northerly in the Atlantic and Indian sectors of the Southern Ocean and more southerly in the Pacific sector. It follows that the SST at the PF is warmer in the Atlantic and Indian sectors and cooler in the Pacific sector [see *Freeman and Lovenduski*, 2016a].

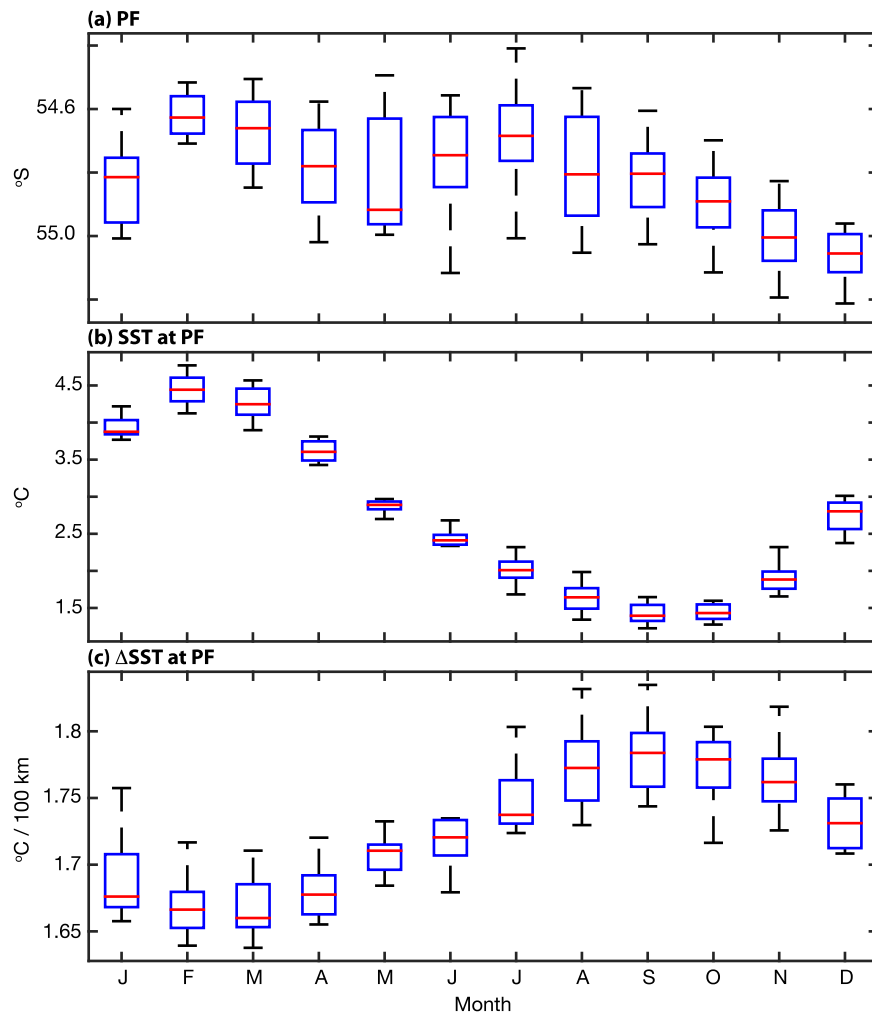


**Figure 2.** The zonal mean (a) Polar Front location and (b) SST and (c)  $\Delta$ SST at the PF by month from June 2002 to February 2014. Each box indicates the median value (center red line), 25th and 75th percentiles (blue edges), and extreme data points (black whiskers) of the given data variable.

### 3.1. Seasonal Variability

We find that the zonally averaged position of the PF does not exhibit significant seasonality, despite seasonal changes in both the zonal mean SST and  $\Delta$ SST identified at the PF (Figure 2). On average, the front resides in its most equatorward position in both February and July and contracts poleward throughout the spring months. In late austral summer-early autumn, frontal temperatures are the warmest and marked by the weakest gradients (Figures 2b and 2c). Conversely, during late winter-early spring, SSTs are cold and the PF is characterized by strong temperature gradients (Figures 2b and 2c). Indeed, temporal variability in the zonal mean SST at the PF is dominated by the seasonal cycle and varies from  $\sim 4.5^\circ\text{C}$  in February to  $\sim 1.5^\circ\text{C}$  in September. Likewise, temporal variability in the zonal mean  $\Delta$ SST at the PF is dominated by the seasonal cycle, varying from  $\sim 1.67^\circ\text{C}$  per 100 km in February to  $\sim 1.78^\circ\text{C}$  per 100 km in September. In a zonally averaged sense, this seasonal behavior is consistent with the findings of Moore *et al.* [1999] and Dong *et al.* [2006].

Unlike the zonal mean position of the PF, in certain regions of the Southern Ocean, the location of the PF is dominated by seasonal variation (Figure 3a). During cold season months (winter-spring), the PF has a more northerly position and during warm season months (summer-fall), the PF has a more southerly position, except in the Indian sector ( $\sim 90^\circ\text{E}$ – $140^\circ\text{E}$ ), where the PF tends to shift north when temperatures are warmer. In the western Pacific, south of New Zealand, the PF shifts equatorward during the cold season and poleward during the warm season. We find that seasonally dominated regions are characterized by deep ocean depths (Figure 3a; e.g.,  $\sim 50^\circ\text{E}$ ,  $120^\circ\text{E}$ – $140^\circ\text{E}$ ,  $160^\circ\text{E}$ – $180^\circ\text{E}$ ,  $\sim 340^\circ\text{E}$ ; see section 3.2); here the winter-spring paths tend to diverge from the summer-fall paths. For example, the amplitude of the seasonal cycle in the mean PF position within the  $120^\circ\text{E}$ – $140^\circ\text{E}$  region, characterized by ocean depths of  $\sim 4$  km, is  $2.1^\circ$  latitude

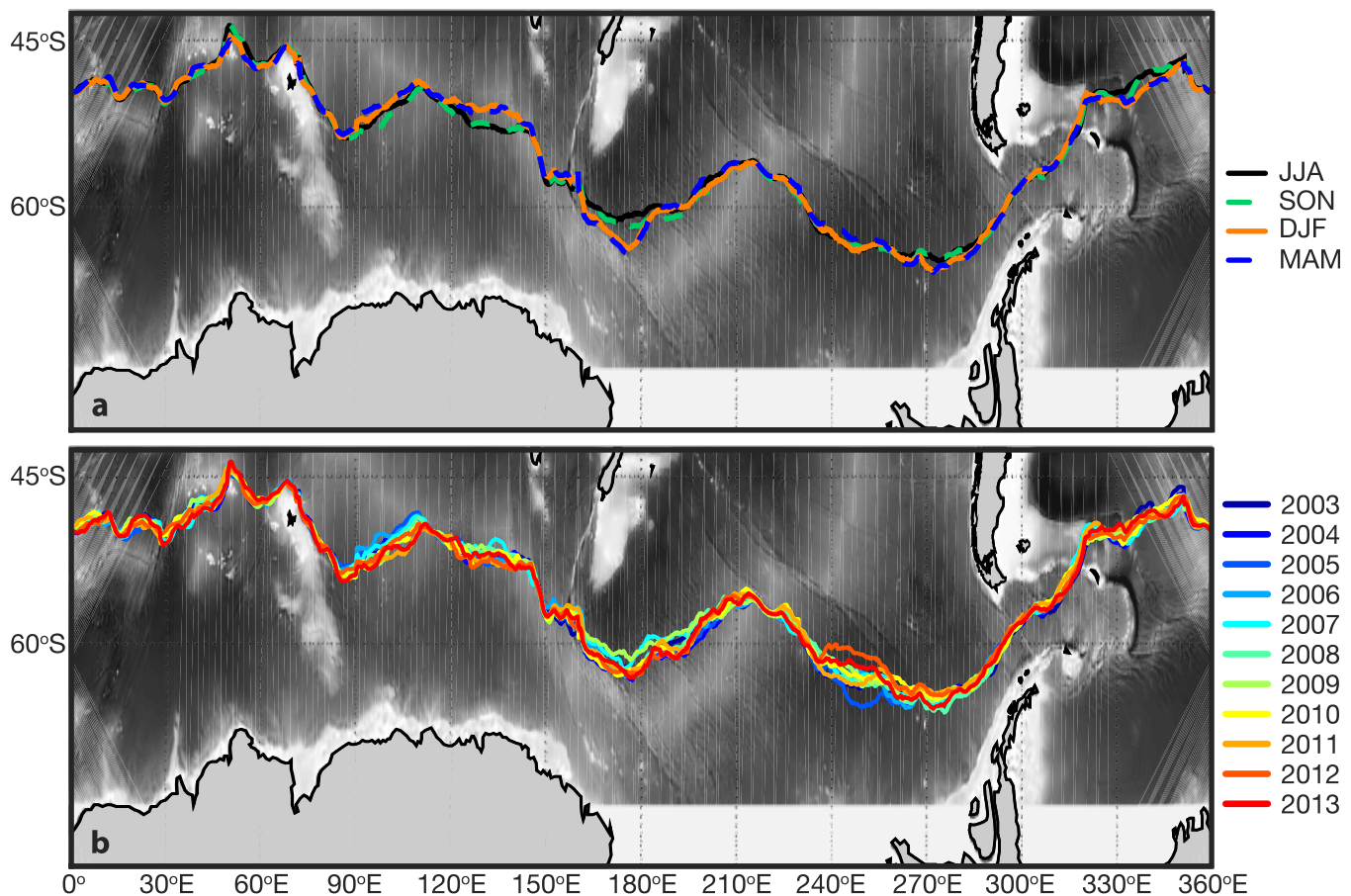


**Figure 3.** (a) Seasonal mean position in the Antarctic Polar Front (June 2002 to February 2014): austral winter (JJA; yellow), spring (SON; blue), summer (DJF; magenta), and fall (MAM; green). (b) Annual mean PF positions (January 2003 to December 2013). Bottom topography (as in Figure 1) displayed underneath PF positions in both plots, where light shading indicates shallow bathymetry and dark shading, deep.

(~235 km), exceeding interannual variability ( $\leq 120$  km standard deviation; Figure 1b), suggesting that the seasonal cycle dominates PF variability in this region. In general, the seasonal variability in the PF presented in this study (Figure 3a) is relatively small when compared to the differences between the many PF climatological mean positions found in past studies [see *Freeman and Lovenduski*, 2016a, Figure 6], suggesting that these differences are not the result of seasonal sampling biases.

### 3.2. Interannual Variability

We find that interannual variability in the PF path is largely determined by bottom topography, consistent with previous PF studies [*Deacon*, 1937; *Gordon et al.*, 1978; *Chelton et al.*, 1990; *Gille*, 1994; *Moore et al.*, 1999; *Dong et al.*, 2006; *Sallée et al.*, 2008], most notably through Drake Passage, on the lee side of Kerguelen Plateau, and upon crossing major ridge systems (e.g., Pacific-Antarctic, Mid-Atlantic, and Southeast Indian Ridges), where seasonal and interannual variability is minimal (Figures 1 and 2). Figure 1b demonstrates that the spatial displacement and temperature variation of the PF is largely constrained by bathymetry: over shallow bathymetry, variability in the location of the PF and its temperature is weak and over deep bathymetry, variability in the location and temperature of the PF is strong (Figure 1). The standard deviation of the latitudinal position of the PF is (a) significantly correlated with the standard deviation in SST at the PF (0.76), (b) significantly correlated with bottom depth (-0.22), and (c) can be as large as 2.0° over deep regions and as small as 0.19° over shallow regions. This topographic influence on seasonal and interannual variability in the PF path can also be seen in Figures 3a and 3b, respectively, where we find a greater spread in the seasonal and annual mean position of the PF over regions characterized by weak topographic influence (e.g., 90°E–110°E and 240°E–270°E). In these regions of weak topographic influence, previous studies have indicated that fronts tend to be associated with multiple filaments that are often weak [*Sokolov and Rintoul*, 2002; *Graham et al.*, 2012]. Since the mapping technique of *Freeman and Lovenduski* [2016a] preferentially selects the southernmost filament in these multifilament cases, while ensuring spatial and/or thermal continuity, this study tracks only the variability in this filament.

The leading mode of climate variability in the Southern Hemisphere is the Southern Annular Mode (SAM), associated with meridional shifts in the westerlies (e.g., a positive SAM event translates into a poleward shift in the westerly wind jet) [*Thompson and Wallace*, 2000]. The atmospheric circulation of the Southern Hemisphere is also influenced by the high-latitude response to the El Niño-Southern Oscillation (ENSO), associated with anomalous sea level pressure patterns and correlated with various Southern Ocean properties such as sea ice extent, SST, mixed layer depth, and upper-ocean heat content [*Renwick*, 2002; *Sallée et al.*, 2008; *Stephenson et al.*, 2013]. To investigate the influence of the SAM on interannual variability in the PF, we regress the monthly, zonal mean PF position, SST and  $\Delta$ SST at the PF onto the SAM index (see section 2.3), yielding a regression coefficient of -0.27° latitude, -1.97°C, and -7.51°C/100 km per standard deviation change in the index, respectively; see Table 1. Similarly, for the influence of the ENSO on interannual variability in the PF, we regress the monthly, zonal mean PF position, SST and  $\Delta$ SST at the PF onto the ENSO index (see section 2.3), yielding a regression coefficient of -0.62° latitude, 0.93°C, and 2.53°C/100 km per standard deviation change in the index, respectively; see Table 1. Therefore, during positive phases of the SAM, we find a cool, weak, and southerly mean PF. During positive ENSO phases, we find a warm, strong, and southerly mean PF. However, in a zonally averaged sense, the SAM only explains <1% of the monthly variance in the PF, whereas the ENSO explains ~2%.

**Table 1.** Mean Values and Regression and Correlation Coefficients of the Mean Time Series With the SAM and ENSO Index<sup>a</sup>

Variable	Mean Value	Regression Coefficient Associated With $1\sigma_{Index}$		Correlation With Index	
		SAM	ENSO	SAM	ENSO
PF (°latitude)	-54.81	-0.27	-0.62	-0.0543	-0.1336
SST at PF (°C) <sup>b</sup>	2.71	-1.97	0.93	-0.3517 <sup>c</sup>	0.1816
$\Delta$ SST at PF (°C/100 km) <sup>b</sup>	1.73	-7.51	2.53	-0.1571	0.0581

<sup>a</sup>Regression coefficients correspond to one standard deviation change in the given climate index; significant at the 95% level.

<sup>b</sup>Anomalous variable.

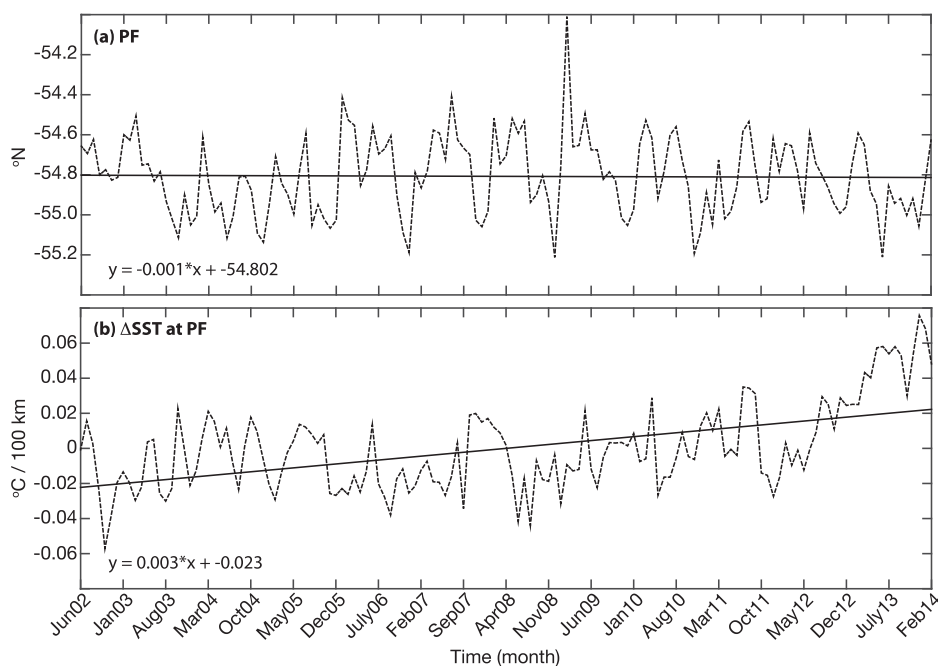
<sup>c</sup>Correlation significant at the 95% level.

### 3.3. Long-Term Trends

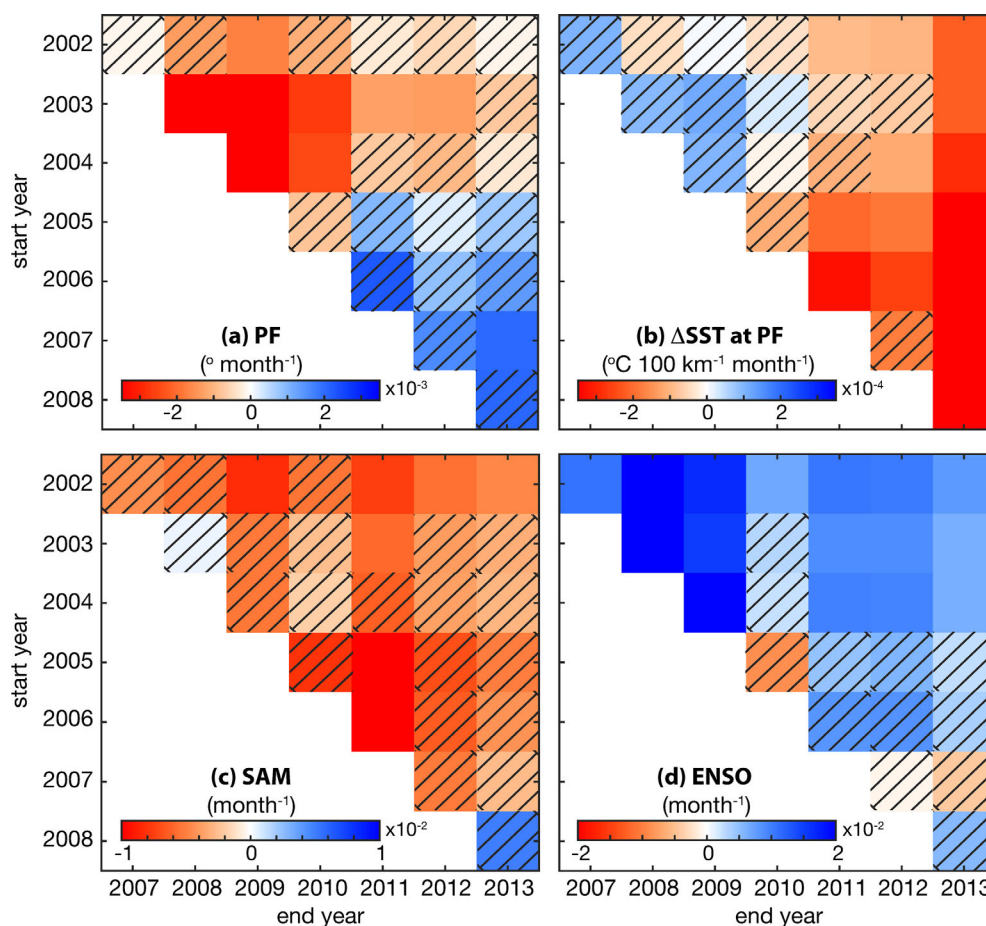
From 2002 to 2014, we find that the trend in the monthly, zonally averaged PF location is near zero (Figure 4a) while the strength of the PF has significantly increased (Figure 4b). We assess the sensitivity of these trends to the start and end points of the time series by calculating trends for a range of start and end years (Figures 5a and 5b): start years ranging from 2002 to 2008 and end years ranging from 2007 to 2013. The sign of the PF intensity trends is robust across many start and end year pairs (Figure 5b), showing that long-term trends in the strength of the PF are independent of start and end year choices. However, a clear switch from a northward shift in the PF location in the beginning of the time series to a southward shift near the end suggests that the long-term trend in the position of the zonal-mean PF is sensitive to the choice of start and end year (Figure 5a).

Figure 6a displays the total change in the PF over the study time period across all longitudes. Regional northward and southward shifts emerge, particularly in the Amundsen Sea sector of the Pacific and in the central/east Indian sector, respectively. These regional trends are also evident in Figure 3b, demonstrating a clear northward displacement in the annual mean front position in the Pacific sector and a southward displacement in the Indian sector. We investigate PF variability in these sectors by creating regional time series: the Pacific time series is calculated by averaging over 230°E–260°E and the Indian time series over 75°E–110°E in order to coincide with the regions of maximum trends. Indeed, we calculate a positive trend (i.e., a northward shift) in frontal position in the Pacific time series and a negative trend (i.e., a southward shift) in the Indian time series over 2002–2014; these statistically significant opposing regional trends combine to produce the near-zero trend in the zonal mean PF (Figure 4a). Correlations between the Pacific and Indian time series (not shown) fail to exceed the 95% confidence level, indicating that different processes may be driving PF variability in these two high trend regions. Trends observed in the Pacific and Indian sectors are dominated by trends in the cold season months (winter-spring; not shown).

A previous study has shown that PF variability in the Pacific and Indian sectors is strongly linked to the SAM and ENSO [Sallée et al., 2008]. In section 3.2, we demonstrate the influence of these phenomena on interannual variability in the zonally averaged PF, but find that these relationships are insufficient in explaining long-term trends. In the Pacific and Indian sectors, we find that the proportion of



**Figure 4.** Time series of monthly, zonal mean (a) Polar Front position and (b) anomalous SST gradient at the PF (dashed) from June 2002 to February 2014. Fitted linear least squares line (solid) and associated slope-intercept equation indicated; fitted line in Figure 4b is significant at the 95% level.



**Figure 5.** Multidecadal trends in monthly, zonal mean (a) Polar Front location and (b) SST gradient at the PF and monthly (c) SAM and (d) ENSO indices. Color indicates the slope of the fitted trend line (in a least squares sense) for each start and end year pair; trends not significant at the 95% level are hatched.

contemporary PF trends that are linearly congruent with the SAM and ENSO is negligible; at most, congruencies peak at  $<2\%$  and  $<5\%$ , respectively, and the residual displays magnitudes comparable to the PF trends (not shown; see section 2.3). These congruency analyses were repeated for all seasons for both indices and, in all cases, trends in the two leading patterns of Southern Hemisphere climate variability were unable to account for a significant component of the 2002–2014 trends in PF location in these regions (not shown).

Long-term trends in the monthly mean SST at the PF at every longitude (not shown) reflect large-scale Southern Ocean SST changes: warming in the Atlantic and western Indian basins and cooling in the central/eastern Indian and Pacific basins (Figure 7). Despite such regional trends in PF location and SST, the intensity of the PF has increased at nearly all longitudes (Figure 6b). We discuss possible mechanisms in section 4.5.

## 4. Discussion

### 4.1. A Changing Southern Ocean

Evidence for significant changes in the Southern Ocean has grown in recent years. The Southern Ocean has warmed and freshened [Gille, 2002; Böning *et al.*, 2008; Gille, 2008; Cai *et al.*, 2010]. Glaciers are rapidly melting in West Antarctica where the ACC flows near the continent [Rignot *et al.*, 2008]. A recent strengthening of the Southern Ocean carbon sink has been found in two observationally based studies [Landschützer *et al.*, 2015; Munro *et al.*, 2015]. A trend toward a more positive SAM in austral summer has been identified (see Figure 5c), leading to strengthened and more poleward westerly winds [Thompson *et al.*, 2000; Thompson

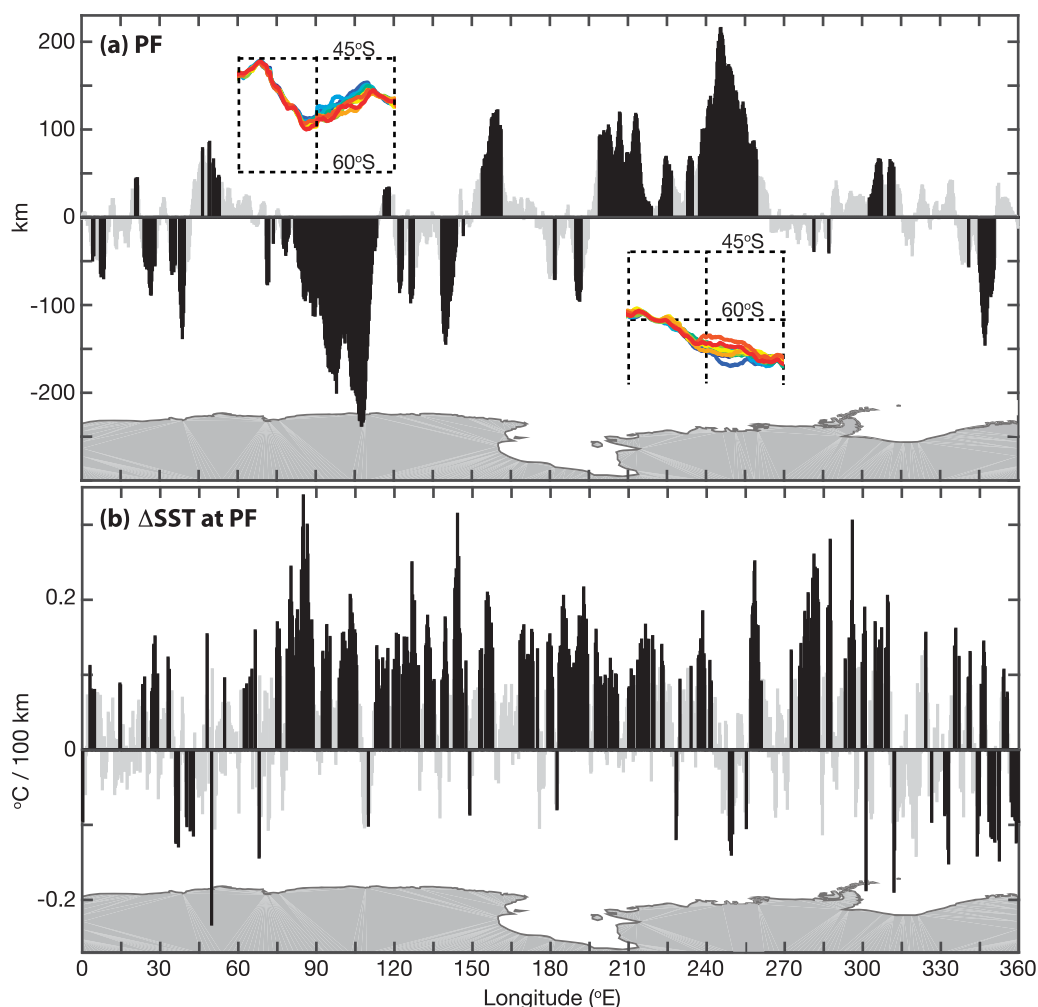


**Figure 6.** Total (a) shift in monthly mean PF location (positive—northward) and (b) change in monthly mean PF intensity (positive—intensified) from June 2002 to February 2014 at every longitude (25 km resolution; black bars indicate significance at the 95% level). Subset plots in Figure 6a are a replication of Figure 3b.

and Wallace, 2001; Marshall, 2003; Thompson *et al.*, 2011]. How the ACC, including its fronts, will respond to future Southern Hemisphere changes is an important question. Some climate models project a continued poleward shift in the westerlies over the next century [Thompson *et al.*, 2011; Swart and Fyfe, 2012; Meijers, 2014] and for the ACC system to mirror them [Fyfe and Saenko, 2006]. However, the combined role of topography, wind, and large-scale climate modes impacting individual ACC fronts both observationally and from a modeling standpoint is an active area of research.

A large portion of the net warming observed in the Southern Ocean has occurred within the circumpolar band of the ACC [Gille, 2008]; multiple studies argue that this concentrated warming is consistent with a southward shift in the ACC itself [Aoki *et al.*, 2003; Sprintall, 2008; Gille, 2008; Morrow *et al.*, 2008]. Alternatively, a warming ACC could result from changes in meridional heat transport (e.g., eddy or surface heat fluxes) and not necessarily from a shift in its position, as suggested by Gille [2014]. Gille [2014] finds no long-term meridional displacement in the zonally averaged latitude of ACC transport, based on analysis of data that are independent of large-scale steric temperature changes. Before our study, the variability and long-term change in the location of the PF within the ACC over this time period of Southern Ocean change was unknown; more specifically, a PF determined without the influence of steric sea level change (see section 2.1), as in Sallée *et al.* [2008], Sokolov and Rintoul [2009b], and Kim and Orsi [2014]. In contrast to such SSH-contour-based measures of PF variability, our study finds no significant meridional displacement in the zonally averaged PF over 2002–2014.

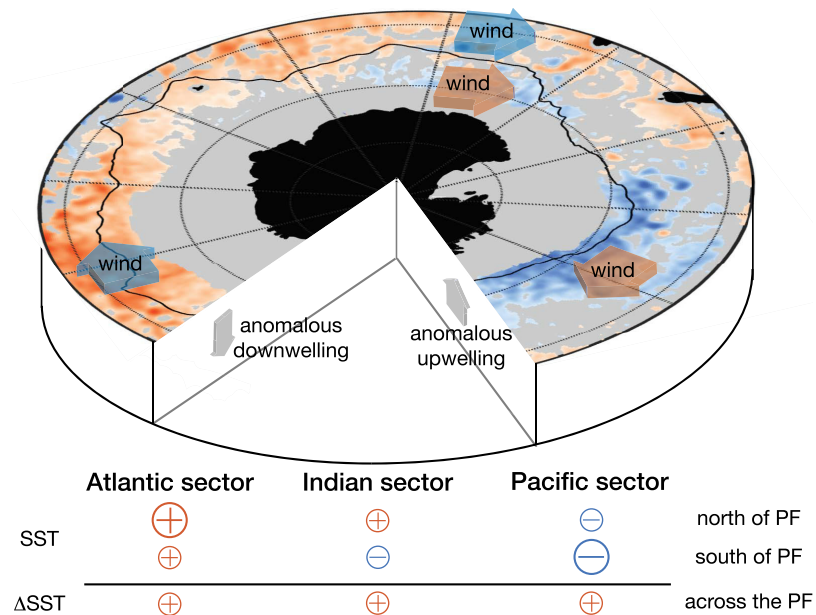


**Figure 7.** Schematic depicting the processes associated with basin-wide frontal intensification since 2002. Stereographic image: the linear trend in monthly microwave SST anomalies from June 2002 to February 2014. The black contour indicates the mean position of the PF. Surface arrows depict changes in the surface wind field over this same period of time. Red colors indicate an increase in SST or surface wind and blue colors indicate a decrease in SST or surface wind over the study time period. Subsurface arrows depict response to changes in surface wind. Figure adapted and modified from Landschützer *et al.* [2015].

#### 4.2. Topographic Influence on the PF

We find a strong relationship between the PF and the underlying bathymetry, a relationship that has been documented frequently and consistently [Deacon, 1937; Gordon *et al.*, 1978; Chelton *et al.*, 1990; Gille, 1994; Moore *et al.*, 1999; Dong *et al.*, 2006; Sokolov and Rintoul, 2007; Sallée *et al.*, 2008]. Moore *et al.* [1999] and Sallée *et al.* [2008] suggest that the position and intensity of the PF are correlated with bathymetry. In order to conserve the barotropic potential vorticity (PV;  $f/h$ ) in the presence of variable ocean depth ( $h$ ), the front is steered to a particular latitudinal location (particular value of  $f$ ), leading to restricted spatial variability. For example, at the shallow Kerguelen Plateau, the PF tends to shift northward to try to conserve PV. Despite this evidence, the extent to which topography determines and controls the PF is still a topic of debate. Sokolov and Rintoul [2009b] shed light on the common misconception regarding topographic steering: while it is accepted that topographic features (i.e., plateaus and ridges) inhibit interannual variability in the PF, this does not necessarily mean that, in the presence of sufficiently strong forcing, the PF cannot shift meridionally in these regions over time.

#### 4.3. Role of Wind

Some studies suggest that away from steep topographic features, where the PF is free to vary across a wide latitudinal range (see sections 3.1 and 3.2), changes in the wind field determine its meridional movements [Howard and Prell, 1992; Sokolov and Rintoul, 2007, 2009a; Dong *et al.*, 2006; Sallée *et al.*, 2008; Kemp *et al.*, 2010]. From a modeling perspective, a change in the position of the overlying surface wind stress has been understood to induce changes in ACC position [Hall and Visbeck, 2002; Oke and England, 2004]. However, the more recent climate change simulations of Graham *et al.* [2012] show that in response to a change in wind-forcing, and in the absence of strong topographic influence (i.e., over flat topography), the location of the PF exhibits significant seasonal variability with little to no long-term meridional displacement, further suggesting that its position within the ACC is not directly controlled by the overlying winds.

In this study, we find a near-zero meridional displacement in both the zonal-mean position of the PF (Figure 4a) and westerly jet (not shown) over the study time period, while both the zonal-mean strength of the PF (Figure 4b) and westerly jet (not shown) have increased. Swart *et al.* [2015] also find a near-zero

trend in annual mean jet position in six wind reanalysis products over their 30 year study period between 1979 and 2009. In the Indian sector (75°E–110°E), a region exhibiting seasonal variability (section 3.1), we find a significant southward displacement in the PF (Figure 6a) and a concurrent decrease in monthly wind speed (not shown). Furthermore, we find a weak positive correlation ( $r = 0.19$ ) between monthly wind speed and PF position in the Indian sector, which suggests that wind may play a small role in determining PF position in this region of weak topographic influence. In the Pacific sector (230°E–260°E), a region also exhibiting seasonal variability (section 3.1), we find a significant northward shift in the PF (Figure 6a) and a concurrent increase in monthly wind speed north of the climatological mean PF position and decrease in monthly wind speed south of the climatological mean PF position (not shown). However, we also find a weak positive correlation ( $r = 0.03$ ) between monthly wind speed and PF position in the Pacific sector.

#### 4.4. Climate Variability Impacts

Large-scale climate modes have also been linked to regional variability and trends in the PF, particularly over flat-bottom areas [Sallée *et al.*, 2008]. The modeling studies of Hall and Visbeck [2002] and Sen Gupta and England [2006] reveal that the wind changes associated with a positive SAM force a southward annual shift of the ACC system, inconsistent with the observed regional responses presented in Sallée *et al.* [2008] which highlight more spatially inhomogeneous frontal variability patterns. Indeed, Sallée *et al.* [2008] show that the SAM dominates PF displacements on short time scales (<3 months), where the latitude of the PF is positively correlated in the Pacific and anticorrelated in the Indian Ocean (i.e., a positive SAM event is associated with a poleward shift in the PF in the Indian sector); on longer time scales (>1 year), the latitude of the PF is anticorrelated with ENSO. This study finds the regional response of the PF to ENSO in the Indo-Pacific sector (110°E–220°E) to be consistent with that of Sallée *et al.* [2008]: a positive ENSO event is associated with a poleward shift in the PF ( $r = -0.27$ ,  $p = 0.00$ ). However, we find weak and insignificant correlations between the position of the PF and the SAM or ENSO indices in their other focus regions; we note that a direct comparison of our results to those of Sallée *et al.* [2008] is hindered by different PF definitions.

#### 4.5. Widespread Frontal Intensification

We have demonstrated that while the zonal-mean position of the PF has not shifted, the front has become more intense across all longitudes during our study period. Previous studies have shown that the atmospheric circulation of the Southern Hemisphere has become increasingly asymmetric since the early 2000s, with conditions more cyclonically dominant in the Pacific sector and more anticyclonically dominant in the Atlantic and parts of the Indian sector. Concurrently, anthropogenic forcing (e.g., stratospheric ozone depletion and greenhouse gas increases) is driving surface circulation changes that vary by region [Haumann *et al.*, 2014]. Therefore, the widespread PF intensification we observe in this study is likely driven by regional changes in temperature and wind, perhaps as a result of this increased asymmetry.

In the Atlantic sector, SSTs have increased more north of the PF and less south of the PF (Figure 7), resulting in an increased SST gradient at the PF over this time period. We find that the strength of the westerly winds and the associated westerly jet have weakened here over this time period (Figure 7), resulting in less Ekman drift; the westerlies drive northward Ekman transport, associated with convergence and downwelling to the north and divergence and upwelling to the south of the maximum wind stress. As a result of the zonally asymmetric atmospheric circulation described above, the Atlantic has experienced surface warming, likely attributed to (1) a reduction in Ekman transport of cold, high-latitude waters to the north (i.e., anomalous downwelling or reduced upwelling; Figure 7) [Landschützer *et al.*, 2015] and (2) increased meridional winds that anomalously advect warm air from the subtropics over the basin, providing surface heating from the atmosphere. Therefore, frontal intensification observed in the Atlantic sector is likely attributed to the thermal response of a more zonally asymmetric atmospheric circulation and a weaker westerly jet.

In the Pacific sector (defined ~210°E–270°E), SSTs have decreased more south of the PF and less north of the PF (Figure 7), resulting in an intensification of the PF since 2002. The observed surface cooling trend in the Pacific can be explained by the more asymmetric atmospheric circulation. Here increased meridional winds, under a more cyclonically dominant pressure system, act to anomalously advect cold air from the Antarctic continent over the basin; changes in sea ice have likely enhanced this surface cooling trend

[Landschützer *et al.*, 2015; Haumann *et al.*, 2014]. In addition, increased westerly winds over the South Pacific suggest enhanced northward Ekman transport (i.e., increased upwelling near the Antarctic continent; Figure 7) [Landschützer *et al.*, 2015]. Taken together, we speculate that the frontal intensification observed in the Pacific sector over this time period is attributed to the thermal response of a more zonally asymmetric atmospheric circulation and stronger westerly winds.

The Indian sector exhibits a relatively weaker signal as compared to the Atlantic and Pacific sectors; the relationship between the zonal wind component and SST appears to dominate the Indian sector, whereas the meridional wind component played a bigger role in the other two sectors (see above). Indeed, the mean westerly jet position coincides with the mean position of the PF. Assuming no significant change in wind direction, in the Indian sector, winds have increased and SSTs have cooled south of the PF (Figure 7), due to increased vertical mixing in the upper ocean. Conversely, winds have decreased and SSTs have warmed north of the PF (Figure 7), due to decreased vertical mixing in the upper ocean. Therefore, we attribute frontal intensification throughout the Indian sector of the Southern Ocean to changes in the strength of the westerly winds.

#### 4.6. The PF on Glacial-Interglacial Time Scales

Reconstructing the position of the PF in past climates is a challenging but important step toward improving our understanding and modeling of glacial-interglacial changes in the climate system and to infer details about the paleo position of the westerlies [Ho *et al.*, 2012; De Deckker *et al.*, 2012; Kohfeld *et al.*, 2013]. PF locations in the paleo record have been identified using water mass properties, but the relative paucity of data available from deep sea cores makes difficult the detection of finer frontal features (e.g., paleo SST gradients). To circumvent these challenges, these methods assume that the SST at the PF is relatively constant in both space and time [Howard and Prell, 1992], yet this study shows that SST varies considerably both spatially and seasonally along the modern-day PF [see also Kostianoy *et al.*, 2004].

Past locations of the PF have also been reconstructed using sedimentary records. Generally, the PF marks the divide between waters replete with silicic acid [Sarmiento *et al.*, 2004] and thus supportive of diatom (opal) productivity, and waters devoid of silicic acid. As such, sedimentary opal tests have been used to demarcate the location of the PF and to infer changes in silicic acid supply and diatom productivity on glacial-interglacial time scales [Anderson *et al.*, 2009; Kemp *et al.*, 2010]. While it is generally agreed that changes in sediment composition occurred in the vicinity of the PF during glacial-interglacial cycles, whether the PF has migrated on these time scales is still an open question [see Kemp *et al.*, 2010, references therein]. This uncertainty highlights a need to further investigate the relationship between the PF and biogeography in the modern-day Southern Ocean [e.g., Chase *et al.*, 2015].

## 5. Conclusions

We quantify the temporal variability in the Antarctic Polar Front using a high-resolution PF data set derived from gradients in the microwave SST record (2002–2014) [Freeman and Lovenduski, 2016b]. Microwave SSTs provide an unimpeded look at the cloudy Southern Ocean and thus allow for the continuous tracking and study of the PF over the past 12 years and, with continued retrievals, the opportunity to extend the PF time series into the future.

In summary, this study finds that the location and intensity of the PF is influenced by bathymetry, acting to reduce its spatial extent and temporal variability over shallow bathymetry. In most locations across the basin, the latitudinal position and intensity of the PF does not vary seasonally yet its temperature exhibits a clear seasonal cycle. From 2002 to 2014, the PF intensifies at nearly all longitudes and two regions of the Southern Ocean experience substantial latitudinal displacements ( $\sim 200$  km): a northward shift in the Pacific sector and a southward shift in the Indian sector. We have investigated the role of SAM and ENSO, the two most dominant modes of large-scale climate variability in the Southern Hemisphere, on the characteristics of the PF and find weak correlations with both phenomena. In zonal average, the PF intensifies with no discernible meridional shift; this basin-wide intensification is possibly a result of observed changes in the westerly wind field and a more zonally asymmetric atmospheric circulation since 2002.

**Acknowledgments**

Weekly PF realizations are available at doi.pangaea.de/10.1594/PANGAEA.855640. Microwave OI SST data are produced by Remote Sensing Systems and sponsored by National Oceanographic Partnership Program (NOPP) and the NASA Earth Science Physical Oceanography Program; data are available at www.remss.com. Microwave radiometer wind speed data are processed by Remote Sensing Systems with funding from the NASA MEaSUREs Program and from the NASA Earth Science Physical Oceanography Program; data are available at www.remss.com. N.M.F. and N.S.L. are grateful for support from NSF (PLR-1543457, OCE-1258995, and OCE-1155240) and NOAA (NA12OAR4310058). NCAR is funded by the National Science Foundation.

**References**

Anderson, R. F., S. Ali, L. I. Bradtmiller, S. H. H. Nielsen, M. Q. Fleisher, B. E. Anderson, and L. H. Burckle (2009), Wind-driven upwelling in the Southern Ocean and the deglacial rise in atmospheric CO<sub>2</sub>, *Science*, 323(5920), 1443–1448, doi:10.1126/science.1167441.

Ansorge, I. J., J. M. Jackson, K. Reid, J. V. Durgadoo, S. Swart, and S. Eberenz (2014), Evidence of a southward eddy corridor in the south-west Indian ocean, *Deep Sea Res., Part II*, 119, 69–76, doi:10.1016/j.dsr2.2014.05.012.

Aoki, S., M. Yoritaka, and A. Masuyama (2003), Multidecadal warming of subsurface temperature in the Indian sector of the Southern Ocean, *J. Geophys. Res.*, 108(C4), 8081, doi:10.1029/2000JC000307.

Belkin, I. M., and A. L. Gordon (1996), Southern Ocean fronts from the Greenwich meridian to Tasmania, *J. Geophys. Res.*, 101, 3675–3696.

Billany, W., S. Swart, J. Hermes, and C. J. C. Reason (2010), Variability of the Southern Ocean fronts at the Greenwich Meridian, *J. Mar. Syst.*, 82, 304–310, doi:10.1016/j.jmarsys.2010.06.005.

Böning, C. W., A. Dispert, M. Visbeck, S. R. Rintoul, and F. U. Schwarzkopf (2008), The response of the Antarctic Circumpolar Current to recent climate change, *Nat. Geosci.*, 1, 864–869, doi:10.1038/ngeo362.

Bretherton, C. S., M. Widmann, V. P. Dymnikov, J. M. Wallace, and I. Bladé (1999), The effective number of spatial degrees of freedom of a time-varying field, *J. Clim.*, 12, 1990–2009, doi:10.1175/1520-0442(1999)012<1990:TENOSD>2.0.CO;2.

Cai, W., T. Cowan, S. Godfrey, and S. Wijffels (2010), Simulations of processes associated with the fast warming rate of the southern Midlatitude Ocean, *J. Clim.*, 23, 197–206, doi:10.1175/2009JCLI3081.1.

Chapman, C. C. (2014), Southern Ocean jets and how to find them: Improving and comparing common jet detection methods, *J. Geophys. Res. Oceans*, 119, 4318–4339, doi:10.1002/2014JC009810.

Chase, Z., K. E. Kohfeld, and K. Matsumoto (2015), Controls on biogenic silica burial in the Southern Ocean, *Global Biogeochem. Cycles*, 29, 1599–1616, doi:10.1002/2015GB005186.

Chelton, D. B., M. G. Schlax, D. L. Witter, and J. G. Richman (1990), Geosat altimeter observations of the surface circulation of the Southern Ocean, *J. Geophys. Res.*, 95, 17,877–17,903, doi:10.1029/JC095iC10p17877.

Deacon, G. E. R. (1937), The hydrology of the Southern Ocean, in *Discovery Reports XV*, pp. 1–124, Cambridge University Press, Fetter Lane, London.

Deacon, G. E. R. (1982), Physical and biological zonation in the Southern Ocean, *Deep Sea Res., Part A*, 29(1), 1–15, doi:10.1016/0198-0149(82)90058-9.

De Deckker, P., M. Moros, K. Perner, and E. Jansen (2012), Influence of the tropics and southern westerlies on glacial interhemispheric asymmetry, *Nat. Geosci.*, 5, 266–269, doi:10.1038/ngeo1431.

de Szoeke, R. A., and M. D. Levine (1981), The advective flux of heat by mean geostrophic motions in the Southern Ocean, *Deep Sea Res., Part A*, 28(10), 1057–1085, doi:10.1016/0198-0149(81)90048-0.

Dong, S., J. Sprintall, and S. T. Gille (2006), Location of the Antarctic Polar Front from AMSR-E Satellite Sea Surface Temperature measurements, *J. Phys. Oceanogr.*, 36, 2075–2089, doi:10.1175/JPO2973.1.

Freeman, N. M., and N. S. Lovenduski (2016a), Mapping the Antarctic Polar Front: Weekly realizations from 2002 to 2014, *Earth Syst. Sci. Data*, 8, 191–198, doi:10.5194/essd-8-191-2016.

Freeman, N. M., and N. S. Lovenduski (2016b), Mapping the Antarctic Polar Front: Weekly realizations from 2002 to 2014, links to NetCDF file and MPEG4 movie, doi:10.1594/PANGAEA.855640.

Fyfe, J. C., and O. A. Saenko (2006), Simulated changes in the extratropical Southern Hemisphere winds and currents, *Geophys. Res. Lett.*, 33, L06701, doi:10.1029/2005GL025332.

Gille, S. T. (1994), Mean sea surface height of the Antarctic Circumpolar Current from Geosat data: Method and application, *J. Geophys. Res.*, 99, 255–273, doi:10.1029/94JC01172.

Gille, S. T. (2002), Warming of the Southern Ocean since the 1950s, *Science*, 295(5558), 1275–1277, doi:10.1126/science.1065863.

Gille, S. T. (2008), Decadal-scale temperature trends in the Southern Hemisphere Ocean, *J. Clim.*, 21, 4749–4765, doi:10.1175/2008JCLI2131.1.

Gille, S. T. (2014), Meridional displacement of the Antarctic Circumpolar Current, *Philos. Trans. R. Soc. A*, 372, 20130273, doi:10.1098/rsta.2013.0273.

Gordon, A. L., E. Molinelli, and T. Baker (1978), Large-scale relative dynamic topography of the Southern Ocean, *J. Geophys. Res.*, 83, 3023–3032, doi:10.1029/JC083iC06p03023.

Graham, R. M., A. M. De Boer, K. J. Heywood, M. R. Chapman, and D. P. Stevens (2012), Southern Ocean fronts: Controlled by wind or topography?, *J. Geophys. Res. Oceans*, 117, C08018, doi:10.1029/2012JC007887.

Hall, A., and M. Visbeck (2002), Synchronous variability in the Southern Hemisphere atmosphere, sea ice, and ocean resulting from the annular mode, *J. Clim.*, 15, 3043–3057, doi:10.1175/1520-0442(2002)015<3043:SVITSH>2.0.CO;2.

Haumann, F. A., D. Notz, and H. Schmidt (2014), Anthropogenic influence on recent circulation-driven Antarctic sea ice changes, *Geophys. Res. Lett.*, 41, 8429–8437, doi:10.1002/2014GL061659.

Ho, M., A. S. Kiem, and D. C. Verdon-Kidd (2012), The Southern Annular Mode: A comparison of indices, *Hydrol. Earth Syst. Sci.*, 16, 967–982, doi:10.5194/hess-16-967-2012.

Howard, W. R., and W. L. Prell (1992), Late quaternary surface circulation of the Southern Indian Ocean and its relationship to orbital variations, *Paleoceanography*, 7, 79–117, doi:10.1029/91PA02994.

Kemp, A. E. S., I. Grigorov, R. B. Pearce, and A. C. Naveira Garabato (2010), Migration of the Antarctic Polar Front through the mid-Pleistocene transition: Evidence and climatic implications, *Quart. Sci. Rev.*, 29, 1993–2009, doi:10.1016/j.quascirev.2010.04.027.

Kim, Y. S., and A. H. Orsi (2014), On the variability of Antarctic Circumpolar Current fronts inferred from 1992–2011 altimetry, *J. Phys. Oceanogr.*, 44, 3054–3071, doi:10.1175/JPO-D-13-0217.1.

Kohfeld, K. E., R. M. Graham, A. M. de Boer, L. C. Sime, E. W. Wolff, C. Le Quééré, and L. Bopp (2013), Southern Hemisphere westerly wind changes during the Last Glacial Maximum: Paleo-data synthesis, *Quart. Sci. Rev.*, 68, 76–95, doi:10.1016/j.quascirev.2013.01.017.

Kostianoy, A. G., A. I. Ginzburg, M. Frankignoulle, and B. Delille (2004), Fronts in the Southern Indian ocean as inferred from satellite sea surface temperature data, *J. Mar. Syst.*, 45, 55–73, doi:10.1016/j.jmarsys.2003.09.004.

Landschützer, P., et al. (2015), The reinvigoration of the Southern Ocean carbon sink, *Science*, 349, 1221–1224, doi:10.1126/science.aab2620.

Langlais, C., S. R. Rintoul, and A. Schiller (2011), Variability and mesoscale activity of the Southern Ocean fronts: Identification of a circumpolar coordinate system, *Ocean Modell.*, 39, 79–96, doi:10.1016/j.ocemod.2011.04.010.

Marshall, G. J. (2003), Trends in the Southern Annular Mode from observations and reanalyses, *J. Clim.*, 16, 4134–4143, doi:10.1175/1520-0442(2003)016<4134:TITSAM>2.0.CO;2.

Marshall, J., and K. Speer (2012), Closure of the meridional overturning circulation through Southern Ocean upwelling, *Nat. Geosci.*, 5, 171–180, doi:10.1038/ngeo1391.

Meijers, A. J. S. (2014), The Southern Ocean in the Coupled Model Intercomparison Project phase 5, *Philos. Trans. R. Soc. A*, 372, 20130296, doi:10.1098/rsta.2013.0296.

- Mignone, B. K., A. Gnanadesikan, J. L. Sarmiento, and R. D. Slater (2006), Central role of Southern Hemisphere winds and eddies in modulating the oceanic uptake of anthropogenic carbon, *Geophys. Res. Lett.*, *33*, L01604, doi:10.1029/2005GL024464.
- Moore, J. K., and M. R. Abbott (2000), Phytoplankton chlorophyll distributions and primary production in the Southern Ocean, *J. Geophys. Res.*, *105*, 28,709–28,722, doi:10.1029/1999JC000043.
- Moore, J. K., M. R. Abbott, and J. G. Richman (1999), Location and dynamics of the Antarctic Polar Front from satellite sea surface temperature data, *J. Geophys. Res.*, *104*, 3059–3073, doi:10.1029/1998JC000032.
- Morrow, R., G. Valladeau, and J. B. Sallée (2008), Observed subsurface signature of Southern Ocean sea level rise, *Prog. Oceanogr.*, *77*(4), 351–366, doi:10.1016/j.pocean.2007.03.002.
- Munro, D. R., N. S. Lovenduski, T. Takahashi, B. B. Stephens, T. Newberger, and C. Sweeney (2015), Recent evidence for a strengthening CO<sub>2</sub> sink in the Southern Ocean from carbonate system measurements in the Drake Passage (2002–2015), *Geophys. Res. Lett.*, *42*, 7623–7630, doi:10.1002/2015GL065194.
- Oke, P. R., and M. H. England (2004), Oceanic response to changes in the latitude of the Southern Hemisphere subpolar westerly winds, *J. Clim.*, *17*, 1040–1054, doi:10.1175/1520-0442(2004)017<1040:ORTCIT>2.0.CO;2.
- Orsi, A. H., T. Whitworth III, and W. D. Nowlin Jr. (1995), On the meridional extent and fronts of the Antarctic Circumpolar Current, *Deep Sea Res., Part I*, *42*(5), 641–673, doi:10.1016/0967-0637(95)00021-W.
- Pollard, R. T., M. I. Lucas, and J. F. Read (2002), Physical controls on biogeochemical zonation in the Southern Ocean, *Deep Sea Res., Part II*, *49*, 3289–3305, doi:10.1016/S0967-0645(02)00084-X.
- Remote Sensing Systems (2016), Monthly mean wind speed data set on a 1 degree grid made from Remote Sensing Systems Version-7 Microwave Radiometer Data, V0701, Santa Rosa, Calif. [Available at [www.remss.com](http://www.remss.com).]
- Renwick, J. A. (2002), Southern Hemisphere Circulation and relations with sea ice and sea surface temperature, *J. Clim.*, *15*, 3058–3068, doi:10.1175/1520-0442(2002)015<3058:SHCARW>2.0.CO;2.
- Rignot, E., J. L. Bamber, M. R. van den Broeke, C. Davis, Y. Li, W. J. van de Berg, and E. van Meijgaard (2008), Recent Antarctic ice mass loss from radar interferometry and regional climate modelling, *Nat. Geosci.*, *1*, 106–110, doi:10.1038/ngeo102.
- Rintoul, S. R., C. Hughes, and D. Olbers (2001), The Antarctic Circumpolar Current system, in *Ocean Circulation and Climate*, edited by G. Siedler, J. Church, and J. Gould, pp. 271–302, Academic Press, San Diego, Calif.
- Sabine, C. L., et al. (2004), The oceanic sink for anthropogenic CO<sub>2</sub>, *Science*, *305*(5682), 367–371, doi:10.1126/science.1097403.
- Sallée, J. B., K. Speer, and R. Morrow (2008), Response of the Antarctic Circumpolar Current to atmospheric variability, *J. Clim.*, *21*(12), 3020–3039, doi:10.1175/2007JCLI1702.1.
- Sallée, J. B., R. J. Matear, S. R. Rintoul, and A. Lenton (2012), Localized subduction of anthropogenic carbon dioxide in the Southern Hemisphere oceans, *Nat. Geosci.*, *5*, 579–584, doi:10.1038/ngeo1523.
- Sarmiento, J. L., N. Gruber, M. A. Brzezinski, and J. P. Dunne (2004), High-latitude controls of thermocline nutrients and low latitude biological productivity, *Nature*, *427*, 56–60, doi:10.1038/nature02127.
- Sen Gupta, A., and M. H. England (2006), Coupled ocean-atmosphere-ice response to variations in the Southern Annular Mode, *J. Clim.*, *19*, 4457–4486, doi:10.1175/JCLI3843.1.
- Smith, W. H., and D. T. Sandwell (1994), Bathymetric prediction from dense satellite altimetry, *J. Geophys. Res.*, *99*, 21,803–21,824, doi:10.1029/94JB00988.
- Sokolov, S., and S. R. Rintoul (2002), Structure of Southern Ocean fronts at 140°E, *J. Mar. Syst.*, *37*, 151–184, doi:10.1016/S0924-7963(02)00200-2.
- Sokolov, S., and S. R. Rintoul (2007), Multiple jets of the Antarctic Circumpolar Current south of Australia, *J. Phys. Oceanogr.*, *37*, 1394–1412, doi:10.1175/JPO3111.1.
- Sokolov, S., and S. R. Rintoul (2009a), Circumpolar structure and distribution of the Antarctic Circumpolar Current fronts: 2. Variability and relationship to sea surface height, *J. Geophys. Res.*, *114*, C11019, doi:10.1029/2008JC005248.
- Sokolov, S., and S. R. Rintoul (2009b), Circumpolar structure and distribution of the Antarctic Circumpolar Current fronts: 1. Mean circumpolar paths, *J. Geophys. Res.*, *114*, C11018, doi:10.1029/2008JC005108.
- Sprintall, J. (2008), Long-term trends and interannual variability of temperature in Drake Passage, *Prog. Oceanogr.*, *77*(4), 316–330, doi:10.1016/j.pocean.2006.06.004.
- Stephenson, G. R., Jr., S. T. Gille, and J. Sprintall (2013), Processes controlling upper-ocean heat content in Drake Passage, *J. Geophys. Res. Oceans*, *118*, 4409–4423, doi:10.1002/jgrc.201315.
- Swart, N. C., and J. C. Fyfe (2012), Observed and simulated changes in the Southern Hemisphere surface westerly wind-stress, *Geophys. Res. Lett.*, *39*, L16711, doi:10.1029/2012GL052810.
- Swart, N. C., J. C. Fyfe, N. Gillett, and G. J. Marshall (2015), Comparing trends in the Southern Annular Mode and surface westerly jet, *J. Clim.*, *28*, 8840–8859, doi:10.1175/JCLI-D-15-0334.1.
- Swart, S., and S. Speich (2010), An altimetry-based gravest empirical mode south of Africa: 2. Dynamic nature of the Antarctic Circumpolar Current fronts, *J. Geophys. Res.*, *115*, C03003, doi:10.1029/2009JC005300.
- Thompson, D. W. J., and J. M. Wallace (2000), Annular modes in the extratropical circulation. Part I: Month-to-month variability, *J. Clim.*, *13*, 1000–1016, doi:10.1175/1520-0442(2000)013<1000:AMITEC>2.0.CO;2.
- Thompson, D. W. J., and J. M. Wallace (2001), Regional climate impacts of the Northern Hemisphere Annular Mode, *Science*, *293*(5527), 85–89, doi:10.1126/science.1058958.
- Thompson, D. W. J., J. M. Wallace, and G. C. Hegerl (2000), Annular modes in the extratropical circulation. Part II: Trends, *J. Clim.*, *13*, 1018–1036, doi:10.1175/1520-0442(2000)013<1018:AMITEC>2.0.CO;2.
- Thompson, D. W. J., S. Solomon, P. J. Kushner, M. H. England, K. M. Grise, and D. J. Karoly (2011), Signatures of the Antarctic ozone hole in Southern Hemisphere surface climate change, *Nat. Geosci.*, *4*, 741–749, doi:10.1038/ngeo1296.
- Wentz, F. J. (2015), A 17-yr climate record of environmental parameters derived from the Tropical Rainfall Measuring Mission (TRMM) Microwave Imager, *J. Clim.*, *28*, 6882–6902, doi:10.1175/JCLI-D-15-0155.1.
- Wentz, F. J., C. Gentemann, D. Smith, and D. Chelton (2000), Satellite measurements of sea surface temperature through clouds, *Science*, *288*, 847–850, doi:10.1126/science.288.5467.847.

## Erratum

In the originally published version of this article, there was a technical error with Figure 5. The figure has since been corrected, and this version may be considered the authoritative version of record.